The Astrophysical Journal Letters, 938:L17 (7pp), 2022 October 20 https://doi.org/10.3847/2041-8213/ac8803

Early Results from GLASS-JWST. V: The First Rest-frame Optical Size–Luminosity Relation of Galaxies at $z > 7$

L. Yang[1], T. Morishita[2], N. Leethochawalit[3,4,5], M. Castellano[6], A. Calabrò[6], T. Treu[7], A. Bonchi[6,8], A. Fontana[6], C. Mason[9,10], E. Merlin[6], D. Paris[6], M. Trenti[3,4], G. Roberts-Borsani[7], M. Bradac[11,12], E. Vanzella[13], B. Vulcani[14], D. Marchesini[15], X. Ding[1], T. Nanayakkara[16], S. Birrer[17,18,19], K. Glazebrook[16], T. Jones[12], K. Boyett[3,4], P. Santini[20], V. Strait[9,10], and X. Wang[2]

[1] Kavli Institute for the Physics and Mathematics of the Universe, The University of Tokyo, Kashiwa, 277-8583 Japan; lilan.yang@ipmu.jp
[2] Infrared Processing and Analysis Center, Caltech, 1200 E. California Blvd., Pasadena, CA 91125, USA
[3] School of Physics, University of Melbourne, Parkville, 3010, VIC, Australia
[4] ARC Centre of Excellence for All Sky Astrophysics in 3 Dimensions (ASTRO 3D), Australia
[5] National Astronomical Research Institute of Thailand (NARIT), Mae Rim, Chiang Mai, 50180, Thailand
[6] INAF Osservatorio Astronomico di Roma, Via Frascati 33, 00078 Monteporzio Catone, Rome, Italy
[7] Department of Physics and Astronomy, University of California, Los Angeles, 430 Portola Plaza, Los Angeles, CA 90095, USA
[8] ASI-Space Science Data Center, Via del Politecnico, I-00133 Roma, Italy
[9] Cosmic Dawn Center (DAWN), Denmark
[10] Niels Bohr Institute, University of Copenhagen, Jagtvej 128, DK-2200 Copenhagen N, Denmark
[11] University of Ljubljana, Department of Mathematics and Physics, Jadranska ulica 19, SI-1000 Ljubljana, Slovenia
[12] Department of Physics and Astronomy, University of California Davis, 1 Shields Avenue, Davis, CA 95616, USA
[13] INAF - OAS, Osservatorio di Astrofisica e Scienza dello Spazio di Bologna, via Gobetti 93/3, I-40129 Bologna, Italy
[14] INAF Osservatorio Astronomico di Padova, vicolo dell'Osservatorio 5, 35122 Padova, Italy
[15] Department of Physics and Astronomy, Tufts University, 574 Boston Ave., Medford, MA 02155, USA
[16] Centre for Astrophysics and Supercomputing, Swinburne University of Technology, PO Box 218, Hawthorn, VIC, 3122, Australia
[17] Kavli Institute for Particle Astrophysics and Cosmology and Department of Physics, Stanford University, Stanford, CA 94305, USA
[18] SLAC National Accelerator Laboratory, Menlo Park, CA 94025, USA
[19] Department of Physics and Astronomy, Stony Brook University, Stony Brook, NY 11794, USA
[20] INAF - Osservatorio Astronomico di Roma, via di Frascati 33, 00078 Monte Porzio Catone, Italy

Received 2022 July 26; revised 2022 August 4; accepted 2022 August 8; published 2022 October 18

Abstract

We present the first rest-frame optical size–luminosity relation of galaxies at $z > 7$, using the NIRCam imaging data obtained by the GLASS James Webb Space Telescope Early Release Science (GLASS-JWST-ERS) program, providing the deepest extragalactic data of the ERS campaign. Our sample consists of 19 photometrically selected bright galaxies with $m_{\mathrm{F444W}} \leqslant 27.8$ at $7 < z < 9$ and $m_{\mathrm{F444W}} < 28.2$ at $z \sim 9-15$. We measure the size of the galaxies in five bands, from rest-frame optical (∼4800 Å) to the UV (∼1600 Å) based on the Sérsic model, and analyse the size–luminosity relation as a function of wavelength. Remarkably, the data quality of the NIRCam imaging is sufficient to probe the half-light radius r_e down to ∼100 pc at $z > 7$. Given the limited sample size and magnitude range, we first fix the slope to that observed for larger samples in rest-frame UV using Hubble Space Telescope samples. The median size r_0 at the reference luminosity $M = -21$ decreases slightly from rest-frame optical (600 ± 80 pc) to UV (450 ± 130 pc). We then refit the size–luminosity relation allowing the slope to vary. The slope is consistent with $\beta \sim 0.2$ for all bands except F150W, where we find a marginally steeper slope of $\beta = 0.53 \pm 0.15$. The steep UV slope is mainly driven by the smallest and faintest galaxies. If confirmed by larger samples, it implies that the UV size–luminosity relation breaks toward the faint end, as suggested by lensing studies.

Key words: Galaxy evolution

1. Introduction

The size of a galaxy is a fundamental observable quantity. Its evolution and scaling relation with other properties such as luminosity and stellar mass provide important clues on the formation and evolution of galaxies across cosmic time (Conselice 2014).

At $z > 7$, the study of the size–luminosity relation has been limited so far to rest-frame UV wavelengths due to a lack of high-resolution imaging beyond the near-infrared bands. The nature of the size and size–luminosity relation in rest-frame optical still remains an open question. Numerical studies predict a range of options for how the size of galaxies varies between the UV and optical bands. Ma et al. (2018) predicted that galaxy sizes measured in rest-frame UV are smaller than those in optical because UV emission tends to trace clumpy star-forming regions, while Wu et al. (2020) predicted similar sizes in the two bands. In contrast, Marshall et al. (2022) and Roper et al. (2022) found that the perceived size of galaxies at rest-frame UV is larger than in redder bands due to the concentration of dust in central regions. They predicted that the slope in the rest-frame optical band should be flatter than that in the UV band at these redshifts.

The UV sizes of $z > 7$ galaxies (defined by the half-light radius, r_e) are compact and marginally resolved by the Hubble Space Telescope (HST). Many studies have analysed UV galaxy sizes and the UV size–luminosity relation at $z > 7$, expressed by the parameterization $r_e \propto L^{\beta}$. Using HST data, Shibuya et al. (2015) found an index of $\beta = 0.27 \pm 0.01$ across redshift range $z = 0{-}8$, which is consistent with many others (Grazian et al. 2012; Huang et al. 2013; Ono et al. 2013; Holwerda et al. 2015), and a median size of $r_0 \sim 420$ pc at $z \sim 8$ at an absolute magnitude of $M_{\rm UV} = -21.0$. The magnification power of gravitational lensing can boost the effective resolution of HST (Kawamata et al. 2018; Bouwens et al. 2022; Yang et al. 2022), but it cannot lift the limitation in wavelength coverage.

The James Webb Space Telescope (JWST) is revolutionizing our understanding of galaxies at $z > 7$ by providing unprecedented depth and spatial resolution at both rest-frame optical and UV wavelengths. The NIRCam filter F444W enables us to probe the rest-frame optical size of galaxies at $z > 7$ at a similar angular resolution to that provided by HST WFC3-IR in the rest-frame UV, i.e., F160W. Based on observations from the GLASS James Webb Space Telescope Early Release Science (GLASS-JWST-ERS) program (Treu et al. 2022a), we present the first measurement of the size of bright galaxies at $z > 7$ across multiple broadband wavelengths. We derive their size–luminosity relation as a function of wavelength from rest-frame optical to UV.

For this study, we limit ourselves to relatively bright/high signal-to-noise (S/N) galaxies, which alleviates the potential impact of incompleteness. A more sophisticated analysis, including the full GLASS-JWST data set (i.e., the other half part of the data will be achieved in the near future; see the details in Section 2), a treatment of incompleteness, and evolutionary trends, is deferred to a forthcoming paper. A companion paper in this focus issue examines the wavelength dependency of morphological features such as clumpiness and asymmetry for the same sample (Treu et al. 2022b).

We adopt a standard cosmology with $\Omega_{\rm m} = 0.3$, $\Omega_\Lambda = 0.7$, and $\rm H_0 = 70\,km\,s^{-1}\,Mpc^{-1}$, and the AB magnitude system (Oke & Gunn 1983; Fukugita et al. 1996).

2. JWST Program and Sample Selection

2.1. GLASS-JWST-ERS Program

The GLASS-JWST-ERS program is obtaining the deepest ERS observations with NIRISS, NIRSpec, and NIRCam (Doyon et al. 2012; Jakobsen et al. 2022; Ferruit et al. 2022; Rieke et al. 2005). In primary mode, it is obtaining NIRISS and NIRSpec spectroscopy of galaxies lensed by the HFF cluster Abell 2744 in the cluster core field (see the details in Paper I; Roberts-Borsani et al. 2022). In parallel mode, it is obtaining NIRCam imaging of galaxies in two flanking fields, i.e., 3–8 arcminutes away from the center of the cluster, to NIRISS and NIRSpec, respectively. We refer the reader to Treu et al. (2022a) for details about the program and the observational strategy. GLASS-JWST-ERS utilizes seven filters in NIRCam, four filters in the short-wavelength channel (F090W, F115W, F150W, and F200W) and three filters (F277W, F356W and F444W) in the long-wavelength channel.

In this letter, we focus on the NIRCam data obtained in parallel with NIRISS on 2022 June 28–29. The data are described in more detail by Merlin et al. (2022; hereafter, Paper II). Modest lensing magnification is expected to present in the parallel fields (Medezinski et al. 2016; Bergamini et al. 2022), so that the sizes and luminosities should be considered as upper limits. In this first analysis, we neglect this effect. The issue will be revisited after the completion of the campaign.

2.2. Sample Selection

Our sample is composed of the combination of two photometrically selected galaxy samples, of galaxies at $7 < z < 9$ (Leethochawalit et al. 2022; hereafter, Paper X) and of galaxies at $z \sim 9{-}15$ (Castellano et al. 2022; hereafter, Paper III). The samples are selected from the photometric catalog of Merlin et al. (2022; hereafter, Paper II). We refer the reader to Paper II for details of the image reduction and photometry.

Taking advantage of multiple filters, the catalogs employ the Lyman-break dropout technique and photometric redshift selection to make a robust selection of galaxies at $z > 7$. Both catalogs require $>8\sigma$ detection in F444W to ensure high purity of the selected candidates. The contamination rate of low-z galaxies is expected to be $<10\%$. Based on the two catalogs, our sample consists of 13 galaxies at $7 < z < 9$ and galaxies at $z \sim 9{-}15$. Their $m_{\rm F444W}$ limits are $\leqslant 27.8$ and <28.2, respectively.

3. Size Measurement

To measure the size of each galaxy, we utilize the `python` software `Galight`[21] (Ding et al. 2020). The code inherits the image modeling capabilities of `Lenstronomy` (Birrer et al. 2015; Birrer & Amara 2018; Birrer et al. 2021), and adopts a forward modeling technique to measure the sizes of galaxies. The sizes derived by `Galight/Lenstronomy` are robust, as demonstrated by Kawinwanichakij et al. (2021) and Yang et al. (2021), and the results are consistent with those measured by traditional software such as `GALFIT` (Peng et al. 2002).

We model the light distribution of the sources assuming a Sérsic light profile (Sersic 1968):

$$I(r) = I_0 \exp\left[-b_n\left(\frac{r}{r_e}\right)^{\frac{1}{n_{\rm sérsic}}} - 1\right], \tag{1}$$

where I_0 is the surface brightness amplitude at the half-light radius $r_{\rm e}$ and b_n is a constant related to the Sérsic index $n_{\rm sérsic}$. We adopt the definition $r = \sqrt{x^2 + y^2/q^2}$, where the coordinates (x, y) depend on the position angle and the center position of the light, and q is the axial ratio. In addition, we stack several bright stars in the same field and use it as a point-spread function (PSF) in the forward modeling.

We use mosaic images, with a common aligned pixel grid (the pixel size is 31 mas) in each band to measure the size of each galaxy in a $1\farcs6 \times 1\farcs6$ cutout; see the details of mosaic images in Paper II. We fix $n_{\rm sérsic}$ to 1, which is appropriate for star-forming galaxies (Morishita et al. 2014; Shibuya et al. 2015), and the axial ratio is limited to the range 0.1–1. In some cases, the cutout includes contamination, and we mask out or fit contaminants by additional Sérsic light profiles. We apply the same strategy to fit the galaxies in each band independently. We visually inspect the fitting result for each galaxy in the sample in each band. We flag and remove the bands in which we are not confident of the size measurement owing to a poor fit, edge effects, or defects. Our results are summarized in Table 1.

---

[21] https://github.com/dartoon/galight

Table 1

Size and Luminosity of Galaxies at $z > 7$ Measured from the Rest-frame Optical to the UV Band

ID	RA	Dec	$z_{\rm ph}$	$r_{e,\rm F444W}$ (kpc)	$M_{\rm F444W}$	$r_{e,\rm F356W}$ (kpc)	$M_{\rm F356W}$	$r_{e,\rm F277W}$ (kpc)	$M_{\rm F277W}$	$r_{e,\rm F200W}$ (kpc)	$M_{\rm F200W}$	$r_{e,\rm F150W}$ (kpc)	$M_{\rm F150W}$	$M_{\rm UV}$[c]
1470	3.5137	−30.3628	7.65	0.66 ± 0.09	−19.0 ± 0.13	0.59 ± 0.11	−18.9 ± 0.13	0.46 ± 0.12	−18.2 ± 0.26	0.69 ± 0.20[b]	−18.6 ± 0.32	⋯	⋯	−18.7 ± 0.25
2236	3.4899	−30.3545	7.99	0.20 ± 0.04	−18.8 ± 0.12	0.12 ± 0.05[b]	−17.9 ± 0.24	0.18 ± 0.07[b]	−18.4 ± 0.30	0.14 ± 0.04	−18.5 ± 0.31	0.11 ± 0.03[b]	−18.6 ± 0.27	−18.7 ± 0.20
2574	3.4955	−30.3508	7.38	0.45 ± 0.06	−19.3 ± 0.13	0.39 ± 0.06	−19.3 ± 0.08	0.39 ± 0.08	−19.0 ± 0.12	0.43 ± 0.07	−19.4 ± 0.13	0.34 ± 0.06	−18.9 ± 0.17	−19.2 ± 0.15
2911	3.5118	−30.3468	6.94	0.46 ± 0.02	−20.7 ± 0.04	0.43 ± 0.02	−20.7 ± 0.02	0.36 ± 0.03	−20.1 ± 0.05	0.36 ± 0.05	−19.9 ± 0.09	0.23 ± 0.03	−19.5 ± 0.10	−19.5 ± 0.15
2936	3.5119	−30.3467	7.23	0.61 ± 0.04	−20.0 ± 0.07	0.61 ± 0.04	−20.0 ± 0.05	0.68 ± 0.06	−19.8 ± 0.08	0.90 ± 0.13	−19.7 ± 0.14	0.62 ± 0.11	−19.5 ± 0.15	−19.4 ± 0.30
3120	3.5203	−30.3439	7.45	0.64 ± 0.06	−19.7 ± 0.07	0.92 ± 0.11	−19.9 ± 0.08	0.73 ± 0.08	−19.8 ± 0.09	0.67 ± 0.08	−19.7 ± 0.12	0.67 ± 0.11	−19.5 ± 0.15	−20.1 ± 0.20
4542	3.4880	−30.3254	8.97	0.47 ± 0.07	−19.4 ± 0.12	0.17 ± 0.09	−18.6 ± 0.19	0.40 ± 0.10[b]	−19.2 ± 0.13	0.14 ± 0.03	−18.9 ± 0.18	0.10 ± 0.02	−19.0 ± 0.17	−19.5 ± 0.15
4863	3.4867	−30.3272	8.07	0.24 ± 0.05	−19.3 ± 0.12	0.35 ± 0.09	−18.9 ± 0.12	0.20 ± 0.09	−18.7 ± 0.14	0.27 ± 0.04	−19.3 ± 0.12	0.18 ± 0.03	−19.2 ± 0.15	−19.3 ± 0.10
5001	3.4997	−30.3177	8.10	1.01 ± 0.20	−19.6 ± 0.13	1.40 ± 0.22	−19.5 ± 0.18	3.14 ± 1.10[b]	−19.8 ± 0.23	1.07 ± 0.28	−19.7 ± 0.20	1.23 ± 0.32[b]	−19.9 ± 0.18	−19.4 ± 0.15
1708	3.4906	−30.3604	7.83	0.52 ± 0.03	−20.1 ± 0.09	1.04 ± 0.85[b]	−19.7 ± 0.47	0.41 ± 0.06	−19.5 ± 0.09	0.32 ± 0.04	−19.5 ± 0.12	⋯	⋯	−19.5 ± 0.20
4397	3.4747	−30.3226	8.06	0.87 ± 0.08	−19.9 ± 0.14	0.34 ± 0.35[b]	−18.6 ± 0.79	0.65 ± 0.15[b]	−19.1 ± 0.18	1.11 ± 0.11	−19.8 ± 0.17	⋯	⋯	−19.4 ± 0.25
6116	3.5046	−30.3079	8.24	0.32 ± 0.05	−19.4 ± 0.09	0.72 ± 0.19[b]	−19.1 ± 0.16	4.34 ± 0.49[b]	−20.4 ± 0.24	⋯	⋯	0.40 ± 0.28[b]	−18.4 ± 0.27	−18.8 ± 0.30
6263	3.4697	−30.3090	8.21	0.54 ± 0.07	−19.5 ± 0.14	0.95 ± 0.76[b]	−19.5 ± 0.45	0.39 ± 0.12	−19.1 ± 0.16	0.37 ± 0.10[b]	−19.2 ± 0.15	⋯	⋯	−19.3 ± 1.90
560[c]	3.5119	−30.3718	10.63	0.50 ± 0.02	−21.2 ± 0.05	0.46 ± 0.02	−21.0 ± 0.09	0.49 ± 0.03	−21.0 ± 0.11	0.43 ± 0.02	−21.0 ± 0.15	0.37 ± 0.03	−20.6 ± 0.20	−21.0 ± 0.06
5153[c]	3.4990	−30.3248	12.30	0.17 ± 0.02	−20.4 ± 0.04	0.10 ± 0.02	−20.4 ± 0.06	0.12 ± 0.02	−20.6 ± 0.07	0.12 ± 0.01	−21.1 ± 0.10	⋯	⋯	−21.2 ± 0.20
1351[c]	3.5289	−30.3638	9.33	0.76 ± 0.05	−20.5 ± 0.07	0.78 ± 0.06	−20.7 ± 0.08	0.67 ± 0.08	−20.4 ± 0.13	0.88 ± 0.09	−20.8 ± 0.13	0.68 ± 0.15	−19.7 ± 0.44	−20.7 ± 0.09
2488[c]	3.5137	−30.3516	9.93	2.01 ± 0.37[b]	−19.9 ± 0.12	1.07 ± 0.34	−19.4 ± 0.28	0.39 ± 0.14[b]	−18.9 ± 0.32	0.39 ± 0.09	−19.3 ± 0.34	⋯	⋯	−20.0 ± 0.27
4131[c]	3.4944	−30.3076	9.20	0.28 ± 0.11[b]	−18.5 ± 0.08	0.17 ± 0.07[b]	−18.6 ± 0.09	0.19 ± 0.12[b]	−17.9 ± 0.11	0.21 ± 0.08[b]	−18.9 ± 0.19	0.16 ± 0.07[b]	−18.7 ± 0.39	−20.2 ± 0.18
5889[c]	3.4791	−30.3149	9.05	0.63 ± 0.12	−19.4 ± 0.11	0.39 ± 0.11	−19.0 ± 0.17	0.52 ± 0.13[b]	−19.1 ± 0.34	0.45 ± 0.09	−19.0 ± 0.49	0.61 ± 0.34[b]	−18.6 ± 0.61	−19.7 ± 0.21

Notes. The columns represent the corresponding catalog ID, coordinates, and photometric redshift, provided in Paper X for galaxies at 7 $<z<$9 and Paper III for galaxies at $z \sim 9-15$, measured half-light radius r_e, and absolute magnitudes in the F444W, F356W, F277W, F200W, and F150W filters, respectively, and $M_{\rm UV}$.

[a] The size measurements are not confident.

[b] The sources from 560–5889 correspond to GHZ1–GHZ6 in Paper III.

[c] $M_{\rm UV}$, rest-frame UV absolute magnitude, calculated in Paper X and Paper III.

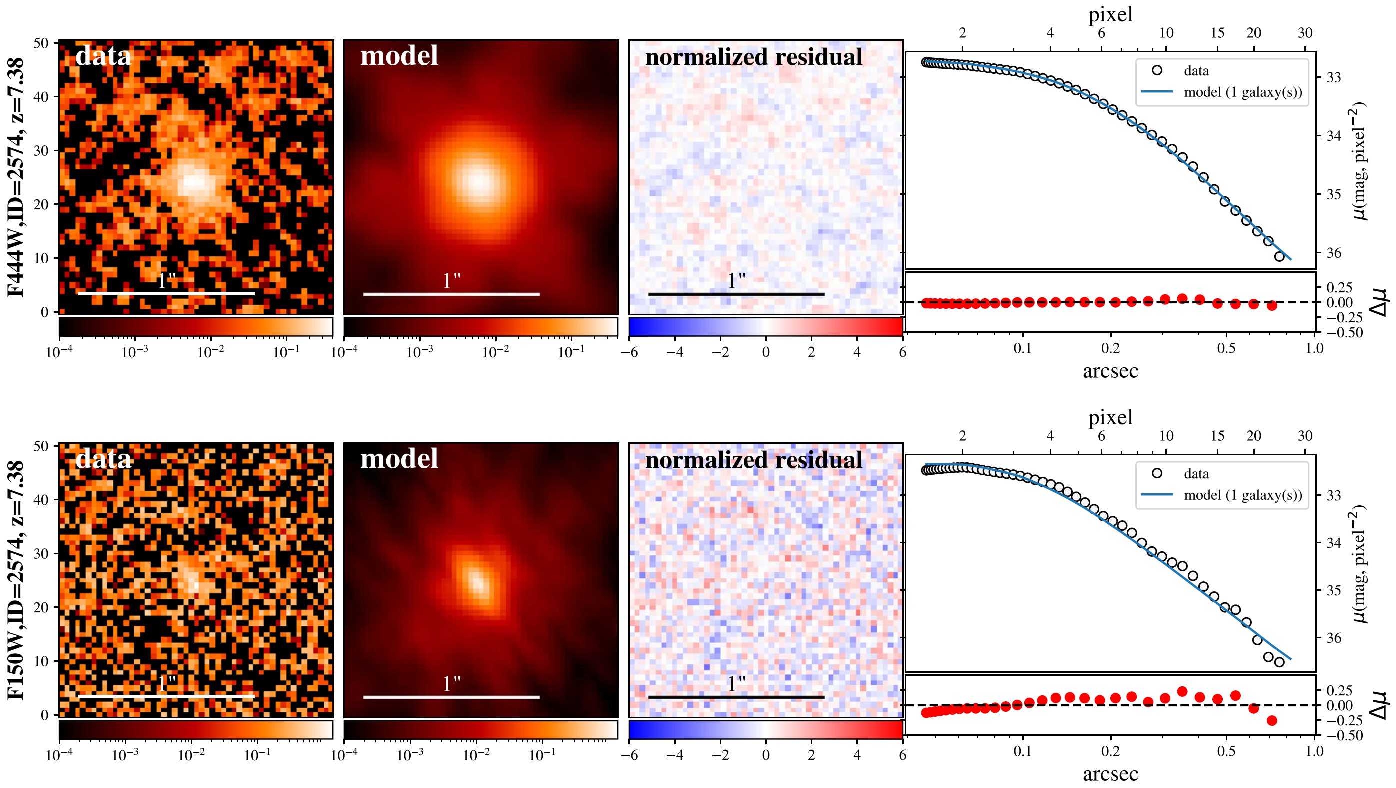

Figure 1. Example of the size measurement of a galaxy (ID = 2574, $z = 7.38$) in the F444W (rest-frame optical; upper) and F150W (UV; bottom) bands using `Galight`. In each panel, from left to right, the columns represent the (1) observed data, (2) best-fit model image, (3) normalized residual map, and (4) surface brightness profiles in 1D and its residuals.

We show an example of the modeling procedures in the rest-frame optical (F444W) and UV (F150W) bands in Figure 1. In general, the galaxies are well fitted by an exponential disk with $n_{\text{sérsic}} = 1$. We also perform the fitting while allowing $n_{\text{sérsic}}$ to vary in the range 0.3–4 and find there is no significant change in size on average (<0.02 dex). A more detailed morphology analysis can be found in a companion paper (Treu et al. 2022b).

4. Size–Luminosity Distribution

In Figure 2, we present the size–luminosity distribution of galaxies at $z > 7$ from the rest-frame optical (∼4800 Å) to UV (∼1600 Å) bands. The source luminosities are calculated from the best-fit magnitudes of our Sérsic fits.

In this Section, we apply an analytic method to derive the size–luminosity relation and report the best-fit results. Given the relatively small sample size at $z > 9$ in this first data set, we do not consider any potential evolution of the intercept with redshift.

4.1. Size–Luminosity Relation in Analytical Form

In order to carry out our fit, we assume that the size distribution at a given luminosity obeys a log-normal function and that the size–luminosity relation can be described by a power law (Shen et al. 2003; Holwerda et al. 2015).

In this way, the probability density function (PDF) of the size–luminosity pair is expressed as:

$$P(r_e, L;\, r_0, \sigma, \beta) = \frac{1}{r_e \sigma \sqrt{2\pi}} \exp\left(-\frac{(\ln r_e - \ln \overline{r_e})^2}{2\sigma^2}\right), \qquad (2)$$

and

$$\overline{r_e} = r_0 \left(\frac{L}{L_0}\right)^{\beta}, \qquad (3)$$

where r$_0$, σ, β, and L_0 are the median radius at L_0, the log-normal dispersion of $\ln r_e$, the slope of the size–luminosity relation, and the characteristic luminosity (corresponding to $M = -21.0$), respectively.

Given the relatively small sample size and narrow brightness range, for our baseline analysis we opt to fix the slope. Since many studies have found consistent UV slopes for entire redshift range (Huang et al. 2013; Ono et al. 2013; Shibuya et al. 2015; Holwerda et al. 2015), we fix the slope to $\beta = 0.20$ as reported by Shibuya et al. (2015) at $z \sim 8$ from HST data. We then use a standard Bayesian approach and run a Markov Chain Monte Carlo (MCMC) process to derive the posterior distributions of parameters r$_0$ and σ.

4.2. The Size–Luminosity Relation as a Function of Wavelength

In each panel of Figure 2, the colored points and lines represent the data and fitting results in the corresponding band, respectively. We performed size measurements on 19, 19, 19, 18, and 13 galaxies in the F444W, F356W, F277W, F200W, and F150W bands, respectively. The failures in F200W and F150W bands are due to a combination of factors: galaxies are out of the detector, have too low S/N (i.e., <1.5), or have an extremely bright contaminant nearby. Some galaxies are not confidently measured, as judged by significant residuals to the Sérsic model fit. Those sources are identified by empty circles; they are shown for completeness and are excluded from the

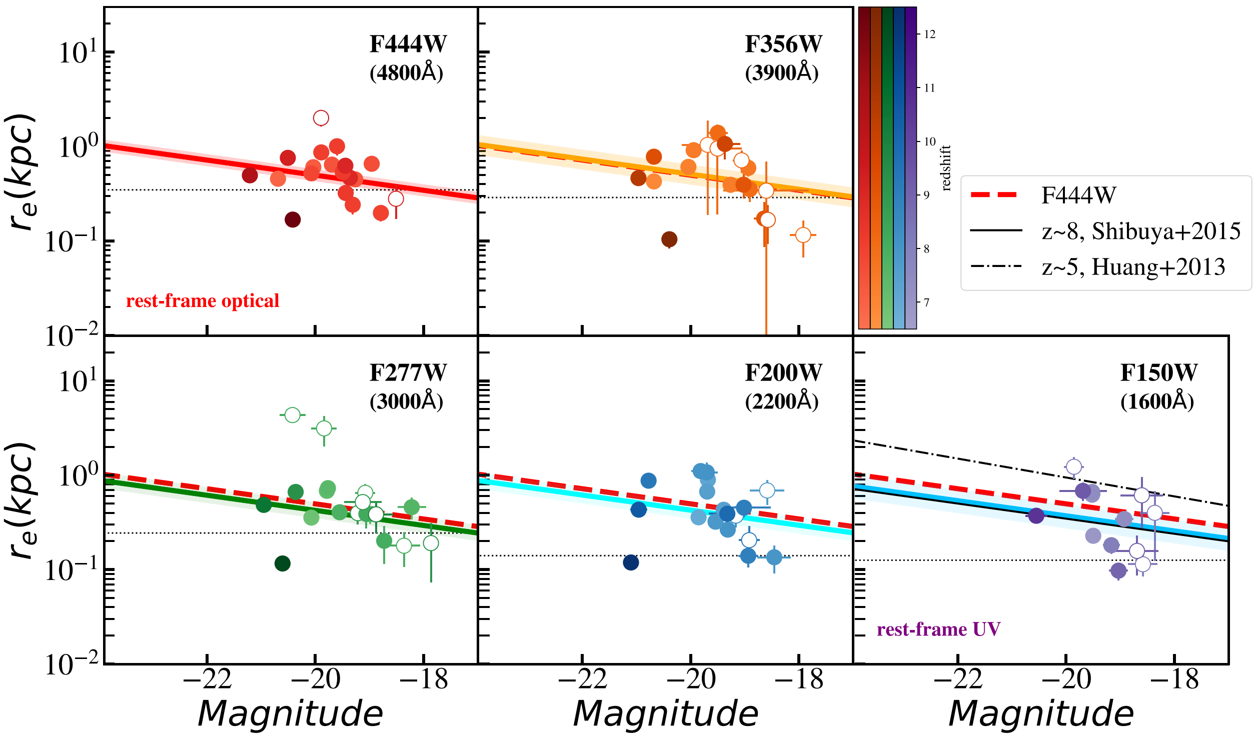

Figure 2. Size–luminosity distribution of galaxies observed in five NIRCam bands from F444W to F150W band, corresponding to rest-frame optical (∼4800 Å) to UV (∼1600 Å). The *x*-axes represent the absolute magnitude measured in each band, and the *y*-axes represent the effective radius measured by `Galight` using the Sérsic model. The solid points, solid lines, and shadow region in each panel represent, respectively, the data, the best fit of the size–luminosity relation, and the 1σ uncertainty range of the derived relation. The color transparency of the data points indicates the redshift. The empty circles show galaxies with less-secure size determinations, displayed here for completeness but not used for fitting. The red dash lines represent the best fits obtained in the F444W band. The black solid and dashed–dotted lines in the F150W panel show the relation derived from HST data by Shibuya et al. (2015; $z \sim 8$) and Huang et al. (2013; $z \sim 5$) at a similar rest-frame wavelength, respectively. The horizontal black dotted line in each panel indicates the PSF size (FWHM/2) for reference.

Table 2
Best-fit Parameters of the Size–Luminosity Relation from the Rest-frame Optical to UV at $z > 7$

Filter	λ	$\log_{10} r_0$/kpc	σ
F444W	4800 Å	−0.22 ± 0.06	0.52 ± 0.10
F356W	3900 Å	−0.21 ± 0.10	0.78 ± 0.18
F277W	3000 Å	−0.29 ± 0.08	0.63 ± 0.16
F200W	2200 Å	−0.29 ± 0.08	0.76 ± 0.15
F150W	1600 Å	−0.35 ± 0.12	0.76 ± 0.23

size–luminosity relation fit. Some galaxies are extremely small, i.e., smaller than the PSF size. We performed mock tests using a Sérsic profile to model the galaxies, and it turns out that the radius can be correctly recovered down to half of the PSF size, i.e., ∼30 mas in the F444W band.

We fit our sample galaxies in the size–luminosity plane of each filter in Figure 2. The best-fit parameters are summarized in Table 2. We reiterate that for this initial analysis, we have limited ourselves to relatively bright galaxies of $m_{F444W} < 28$, and have neglected the effects of potential incompleteness bias and lensing magnification. We will revisit these issues in future work, after the completion of the campaign.

The red dash lines indicate the baseline measured in F444W, to provide a comparison of galaxy size at different rest-frame wavelengths. The median size r_0 is ∼450–600 pc, and slightly decreases from 600 pc in rest-frame optical to 450 pc in rest-frame UV. The scatter, $\sigma \sim 0.7$, does not vary significantly across the filters.

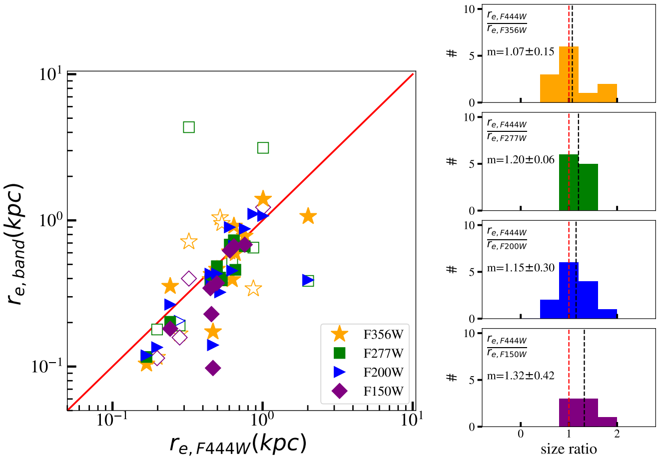

Figure 3. Size comparison among five bands. Left: rest-frame optical (F444W) band size compared to those of the four other bluer bands, i.e., F356W (orange stars), F277W (green squares), F200W (blue triangles), and F150W (purple diamonds). The empty symbols represent those with a less-secure size determination, which are not used for calculating size ratio. Right: histograms of the size ratio distribution between F444W and each of the four bluer bands. In each panel, we indicate the median value of the distribution by the black dash line and reference (size ratio = 1) by the red dash line.

In one of the panels (F150W), we show the best-fit relation of $z \sim 8$ Lyman-break galaxies from Shibuya et al. (2015), measured based on HST images, which is consistent with our results. As a comparison to lower redshift galaxies, we also show the best-fit relation of $z \sim 5$ Lyman-break galaxies from Huang et al. (2013).

Lastly, we compare the sizes obtained from the F444W band to those obtained with the other four bluer bands on an individual basis in Figure 3. In the left panel, we see that the average and median galaxy sizes become smaller at shorter wavelengths, with F150W the most significantly different one. In the right panel, we demonstrate the size ratio distribution and find the median values are 1.07 ± 0.15, 1.20 ± 0.06, 1.15 ± 0.30, and 1.32 ± 0.42 for $r_{e,\mathrm{F444W}}/r_{e,\mathrm{F356W}}$, $r_{e,\mathrm{F444W}}/r_{e,\mathrm{F277W}}$, $r_{e,\mathrm{F444W}}/r_{e,\mathrm{F200W}}$, and $r_{e,\mathrm{F444W}}/r_{e,\mathrm{F150W}}$, respectively.

5. Discussion & Conclusions

In the spirit of a preliminary exploration, we refit the size–luminosity relation allowing the slope to vary. These results should be taken with a grain of salt considering the small sample size. We find that the slopes in F444W, F356W, F277W, F200W, and F150W are 0.19 ± 0.09, 0.25 ± 0.13, 0.17 ± 0.10, 0.30 ± 0.13, and 0.53 ± 0.15, respectively. The slopes in the F444W, F356W F277W, and F200W bands are in agreement with the slope assumed in the analysis above, $\beta \sim 0.2$. However, the slope in F150W (rest UV) is marginally steeper than that, and rather consistent with the results reported from several studies that analysed lensed galaxies in the Hubble Frontier Fields (Kawamata et al. 2018; Bouwens et al. 2022; Yang et al. 2022). We note that the tentative steepening is driven by the smallest and faintest galaxies, which might not be resolved by HST without lensing. If confirmed by larger samples, it would imply that the UV size–luminosity might be a broken power law, i.e., a flatter slope at the brighter end and a steeper slope at the fainter end, as suggested by Bouwens et al. (2022).

We have shown that the median size r_0 decreases slightly from the optical to the far-UV, 600 ± 80 pc to 450 ± 130 pc at $M = -21$. However, we stress that the effect is small and less than we would have expected if the UV emission were confined in a small star-forming region surrounded by a larger envelope of older stars.

The moderate size variation as a function of wavelength is consistent with the analysis of the other morphological parameters, e.g., the Gini structural parameter, M_{20}, concentration, asymmetry, and smoothness, reported in the companion paper by Treu et al. (2022b). We refer the reader to Treu et al. (2022b) for more discussion of the physical interpretation of our findings. We just caution the reader that our results apply to galaxies selected primarily through the Lyman-break technique. Heavily dust obscured or fully quiescent galaxies (if they exist) would not of course be described by our findings.

We also report a tentative detection of a steepening of the slope toward the fainter end in the bluest UV filter.

In the future, after the completion of the campaign, we will revisit this work by including the entire sample, correcting for incompleteness bias, and taking the potential lensing effect into consideration.

This work is based on observations made with the NASA/ESA/CSA James Webb Space Telescope. The data were obtained from the Mikulski Archive for Space Telescopes at the Space Telescope Science Institute, which is operated by the Association of Universities for Research in Astronomy, Inc., under NASA contract NAS 5-03127 for JWST. These observations are associated with program JWST-ERS-1324. We acknowledge financial support from NASA through grant JWST-ERS-1324. L.Y. acknowledges support by JSPS KAKENHI grant No. JP 21F21325. K.G. and T.N. acknowledge support from Australian Research Council Laureate Fellowship FL180100060. M.B. acknowledges support from the Slovenian national research agency ARRS through grant N1-0238. C.M. acknowledges support by the VILLUM FONDEN under grant 37459. The Cosmic Dawn Center (DAWN) is funded by the Danish National Research Foundation under grant DNRF140.

ORCID iDs

L. Yang https://orcid.org/0000-0002-8434-880X
T. Morishita https://orcid.org/0000-0002-8512-1404
N. Leethochawalit https://orcid.org/0000-0003-4570-3159
M. Castellano https://orcid.org/0000-0001-9875-8263
A. Calabrò https://orcid.org/0000-0003-2536-1614
T. Treu https://orcid.org/0000-0002-8460-0390
A. Fontana https://orcid.org/0000-0003-3820-2823
C. Mason https://orcid.org/0000-0002-3407-1785
E. Merlin https://orcid.org/0000-0001-6870-8900
D. Paris https://orcid.org/0000-0002-7409-8114
M. Trenti https://orcid.org/0000-0001-9391-305X
G. Roberts-Borsani https://orcid.org/0000-0002-4140-1367
M. Bradac https://orcid.org/0000-0001-5984-0395
E. Vanzella https://orcid.org/0000-0002-5057-135X
B. Vulcani https://orcid.org/0000-0003-0980-1499
D. Marchesini https://orcid.org/0000-0001-9002-3502
X. Ding https://orcid.org/0000-0001-8917-2148
T. Nanayakkara https://orcid.org/0000-0003-2804-0648
S. Birrer https://orcid.org/0000-0003-3195-5507
K. Glazebrook https://orcid.org/0000-0002-3254-9044
T. Jones https://orcid.org/0000-0001-5860-3419
K. Boyett https://orcid.org/0000-0003-4109-304X
P. Santini https://orcid.org/0000-0002-9334-8705
V. Strait https://orcid.org/0000-0002-6338-7295
X. Wang https://orcid.org/0000-0002-9373-3865

References

Bergamini, P., Acebron, A., Grillo, C., et al. 2022, arXiv:2207.09416
Birrer, S., & Amara, A. 2018, PDU, 22, 189
Birrer, S., Amara, A., & Refregier, A. 2015, ApJ, 813, 102
Birrer, S., Shajib, A., Gilman, D., et al. 2021, JOSS, 6, 3283
Bouwens, R. J., Illingworth, G. D., van Dokkum, P. G., et al. 2022, ApJ, 927, 81
Castellano, M., Fontana, A., Treu, T., et al. 2022, arXiv:2207.09436
Conselice, C. J. 2014, ARA&A, 52, 291
Ding, X., Silverman, J., Treu, T., et al. 2020, ApJ, 888, 37
Doyon, R., Hutchings, J. B., Beaulieu, M., et al. 2012, Proc. SPIE, 8442, 84422R
Ferruit, P., Jakobsen, P., Giardino, G., et al. 2022, A&A, 661, A81
Fukugita, M., Ichikawa, T., Gunn, J. E., et al. 1996, AJ, 111, 1748
Grazian, A., Castellano, M., Fontana, A., et al. 2012, A&A, 547, A51
Holwerda, B. W., Bouwens, R., Oesch, P., et al. 2015, ApJ, 808, 6
Huang, K.-H., Ferguson, H. C., Ravindranath, S., & Su, J. 2013, ApJ, 765, 68
Jakobsen, P., Ferruit, P., Alves de Oliveira, C., et al. 2022, A&A, 661, A80
Kawamata, R., Ishigaki, M., Shimasaku, K., et al. 2018, ApJ, 855, 4
Kawinwanichakij, L., Silverman, J. D., Ding, X., et al. 2021, ApJ, 921, 38
Leethochawalit, N., Trenti, M., Santini, P., et al. 2022, arXiv:2207.11135
Ma, X., Hopkins, P. F., Boylan-Kolchin, M., et al. 2018, MNRAS, 477, 219
Marshall, M. A., Wilkins, S., Di Matteo, T., et al. 2022, MNRAS, 511, 5475
Medezinski, E., Umetsu, K., Okabe, N., et al. 2016, ApJ, 817, 24
Merlin, E., Bonchi, A., Paris, D., et al. 2022, arXiv:2207.11701
Morishita, T., Ichikawa, T., & Kajisawa, M. 2014, ApJ, 785, 18
Oke, J. B., & Gunn, J. E. 1983, ApJ, 266, 713
Ono, Y., Ouchi, M., Curtis-Lake, E., et al. 2013, ApJ, 777, 155
Peng, C. Y., Ho, L. C., Impey, C. D., & Rix, H.-W. 2002, AJ, 124, 266
Rieke, M. J., Kelly, D., & Horner, S. 2005, Proc. SPIE, 5904, 1
Roberts-Borsani, G., Morishita, T., Treu, T., et al. 2022, arXiv:2207.11387

Roper, W. J., Lovell, C. C., Vijayan, A. P., et al. 2022, MNRAS, 514, 1921
Sersic, J. L. 1968, Atlas de Galaxias Australes (Cordoba: Observatorio Astronomico)
Shen, S., Mo, H. J., White, S. D. M., et al. 2003, MNRAS, 343, 978
Shibuya, T., Ouchi, M., & Harikane, Y. 2015, ApJS, 219, 15
Treu, T., Calabro, A., Castellano, M., et al. 2022b, arXiv:2207.13527
Treu, T., Roberts-Borsani, G., Bradac, M., et al. 2022a, ApJ, 935, 110
Wu, X., Davé, R., Tacchella, S., & Lotz, J. 2020, MNRAS, 494, 5636
Yang, L., Leethochawalit, N., Treu, T., et al. 2022, MNRAS, 514, 1148
Yang, L., Roberts-Borsani, G., Treu, T., et al. 2021, MNRAS, 501, 1028